Climate imprints during the 'Medieval Climate Anomaly' and the 'Little Ice Age' in marine records from the Alboran Sea basin

V Nieto-Moreno,[1,2,3] **F Martinez-Ruiz,**[2] **S Giralt,**[4] **D Gallego-Torres,**[2,3] **J García-Orellana,**[5] **P Masqué**[5] **and M Ortega-Huertas**[3]

Abstract

An integrated multiproxy analysis from westernmost Mediterranean hemipelagic sediments has provided further insights into natural climate variability and forcing mechanisms in this region during the last two millennia. Two deep-sea marine records, with a robust age model provided by the activity–depth profiles of ^{210}Pb and ^{137}Cs, together with ^{14}C dating, allowed us to perform a detailed reconstruction of paleoenvironmental and paleoceanographic responses during the 'Medieval Climate Anomaly' (MCA), the 'Little Ice Age' (LIA), the Industrial period (IP) and the second-half of the 20th century. Decreasing trends of fluvial-derived element (Si) and a increasing eolian input (Zr/Al ratio) characterized the MCA and the second-half of the 20th century as prevalent dry periods, while generally humid conditions are evidenced during the LIA and the IP, in accordance to a positive and a negative mode of the North Atlantic Oscillation (NAO), respectively (Trouet et al., 2009). The LIA developed as a sequence of successive short and abrupt dry–humid phase alternation. Furthermore, a noteworthy and sharp decrease of redox-sensitive elements (V/Cr and Ni/Co ratios) and coarser sortable silt at AD 1450 and 1950 yr, support more energetic hydrodynamic conditions at this time (oxygenated bottom waters and faster bottom currents), likely promoted by strengthened cooler waters flowing into the Mediterranean Sea.

Introduction

Paleoclimate reconstructions of the past millennia are critical to improve the current understanding of climate variability and predictions of environmental responses to future climate changes (e.g. Bradley et al., 2003; Jones et al., 2001, 2009). Within the last millennium, the 'Medieval Climate Anomaly' (MCA; AD 800–1300 yr) (Hughes and Diaz, 1994; Stine, 1994), previously termed the 'Medieval Warm Period' (MWP) by Lamb (1965), and the subsequent 'Little Ice Age' (LIA; AD 1300–1800 yr) (Bradley and Jones, 1993; Fagan, 2000), gained considerable and increasing interest as they represent recent and distinct periods characterized by notable climatic shifts attributable to natural forcing and to some extent, to widespread human activities (Ruddiman et al., 2011). Growing evidence for widespread temperature anomalies in the Northern Hemisphere defines the MCA as a warm period, contrasting with the LIA, when cooler conditions were reached (Mann et al., 2008, 2009). The increase in temperatures during the MCA was also accompanied by prolonged droughts in North America and the Mediterranean region (Graham et al., 2011; Moreno et al., 2012; Seager et al., 2007). Several attempts have been undertaken to explain the main driving mechanisms behind these anomalies during the last two millennia as well as during the transition between the MCA and the LIA, encompassing a conjunction of natural external forcing mechanisms (solar irradiance and volcanic activity) which resulted in a prolonged reinforcement of ocean–atmosphere positive feedbacks mechanisms (Trouet et al., 2012, and references therein).

In order to improve the understanding of such recent variability, appropriate high-resolution paleoarchives are required. Among them, marine records from the Alboran Sea basin (westernmost Mediterranean) have been revealed as excellent natural archives for paleoclimate and paleoceanographic reconstructions during the

late Holocene (e.g. Martín-Puertas et al., 2010; Nieto-Moreno et al., 2011, 2013). Here, high sedimentation rates have resulted in exceptional analysis resolution previously (100 yr/cm and 30 yr/cm approximately for gravity- and box-cores, respectively). Hence, two well-dated marine box-core records from the northwestern Alboran basin have been selected for a multiproxy approach based on major and trace element-content, grain size distribution, total organic carbon (TOC) content and mineral composition of the sediments. A statistical assessment of the data set was also performed in order to define and characterize the main proxy families subsequently applied for reconstructing paleoclimate and paleoceanographic fluctuations in the western Mediterranean.

Climatological and oceanographic setting

The humidity regime in the western Mediterranean region is controlled by winter precipitation, mainly driven by the North Atlantic Oscillation (NAO), with centres of action in the Icelandic

[1]Biodiversity and Climate Research Centre (BiK-F), Germany
[2]Instituto Andaluz de Ciencias de la Tierra (CSIC-UGR), Spain
[3]Universidad de Granada, Spain
[4]Institute of Earth Sciences Jaume Almera (CSIC), Spain
[5]Universitat Autònoma de Barcelona, Spain

Corresponding author:
V Nieto-Moreno, Biodiversity and Climate Research Centre (BiK-F), Senckenberganlage 25, Frankfurt am Main D-60325, Germany.
Email: Vanesa.Nieto-Moreno@senckenberg.de; vanesanieto@ugr.es
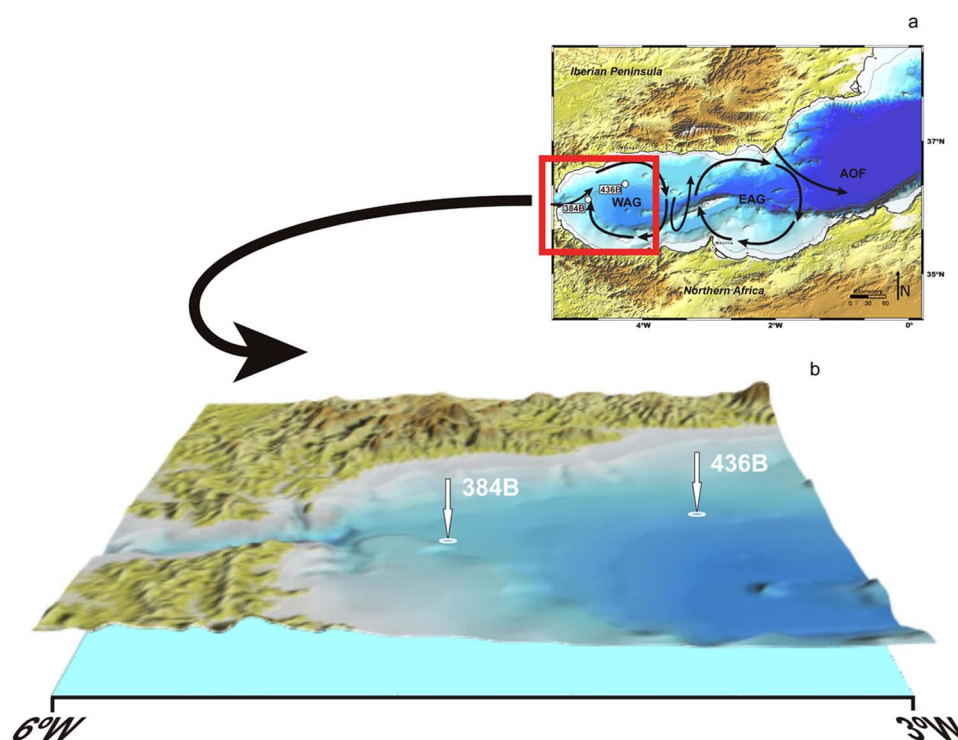
Figure 1. Location of the studied cores in the Alboran basin (a) and bathymetric map showing the main physiographic features of the area under study (b). WAG: Western Alboran gyre; EAG: Eastern Alboran gyre; AOF: Almería-Orán Front.

low and the Azores high and responsible for most of the climatic variability in the North Atlantic (Hurrell, 1995). The NAO alternates between a 'high-index' pattern, characterized by a well-developed and intense Icelandic Low and Azores High, associated with stronger westerlies (and thus higher precipitation) over the eastern North Atlantic and the European continent, and a 'low-index' pattern in which these anomaly cells are rather weak, thus giving rise to reduced westerlies over the eastern North Atlantic and increasing precipitation in the western Mediterranean (Trigo et al., 2002).

In terms of oceanographic setting of the area, the western Mediterranean Sea is characterized by a thermohaline circulation driven by excessive evaporation with respect to precipitation and runoff (e.g. Bethoux, 1979). Hence, the Atlantic jet stream becomes saltier and denser when it flows into the Mediterranean Sea (Modified Atlantic Water, MAW), and two anticyclonic gyres are produced when it progresses eastwards to the Algerian-Balearic Basin (Western and Eastern Alboran Gyres; WAG and EAG) (e.g. Millot, 1999; Perkins et al., 1990) (Figure 1a). The MAW is offset by a deep-water outflow (Mediterranean Outflow Water; MOW) consisting of Levantine Intermediate Water (LIW) and Western Mediterranean Deep Water (WMDW), respectively originated in the Levantine Mediterranean Sea and in the Gulf of Lyon (e.g. Millot, 2008).

## Materials and methods

Sampling

Two box-cores were recovered in the north-western part of the Alboran Sea basin (384B: 35°59.161′N, 4°44.976′W, 1022 m below sea level (b.s.l.) and 436B: 36°12.318′N, 4°18.800′W, 1108 m b.s.l.), using a KP 1.5 box-corer (50 cm × 50 cm × 50 cm) during the Training-Through-Research Cruise 17 (Sagas-08 Cruise), Leg 1, on R/V *Professor Logachev* (Figure 1b). Upon retrieval, box-cores were directly subsampled using PVC pipes (50 cm long and 11.8 cm of internal diameter) inserted into the sediment. Once in the laboratory, one selected core of each box-core was sampled

in 1 cm thick slices. These sediments mainly consist on water-saturated brownish mud in the uppermost 5 cm and homogeneous greyish clay with foraminifera and some shell fragments at the lower part of the cores. Site 384B is c. 110 km east of the Strait of Gibraltar, where the exchange of water between the Mediterranean and the eastern Atlantic takes place, while site 436B is close to the influence of the upwelling cell associated with the northern edge of the WAG (Figure 1a).

Age–depth model

The age–depth model of both cores is based on the activity-depth profiles of ^{210}Pb and ^{137}Cs, plus ^{14}C dating (Figure 2). Determination of ^{210}Pb activities was accomplished through the measurement of its daughter nuclide, ^{210}Po, following the methodology described by Sánchez-Cabeza et al. (1998). Polonium emissions were counted with alpha-spectrometers equipped with low-background silicon surface barrier (SSB) detectors for 4×10^5 s. ^{226}Ra (via ^{214}Pb through its 351 keV gamma emission line) and ^{137}Cs were determined by gamma-spectrometry using a high-purity well-type Ge detector. Excess ^{210}Pb activities were determined by subtracting the ^{226}Ra activity (assumed to equal to the supported ^{210}Pb activity) from the total ^{210}Pb activity (Figure 2a, b; Tables SI and SII, available online).

^{14}C-AMS dates were performed on monospecific planktonic foraminifera (*Globigerina bulloides*) extracted from the >125 μm fraction and analyzed by Accelerator Mass Spectrometry. Radiocarbon ages were calibrated to calendar years (yr AD) using the CALIB 6.0 software (Stuiver and Reimer, 1993) and the MARINE09 curve (Reimer et al., 2009), assuming a global marine reservoir age of 400 yr. Radiocarbon ages were also corrected using a mean regional ΔR value of 108±132, taken from the average of the marine reservoir correction data base of the CALIB software for the western Mediterranean region. Data are reported with a 2σ uncertainty (Figure 2c, d; Table SIII available online). One post-modern sample was converted to yr AD using the CALIBomb software (Reimer et al., 2004) and the calibration
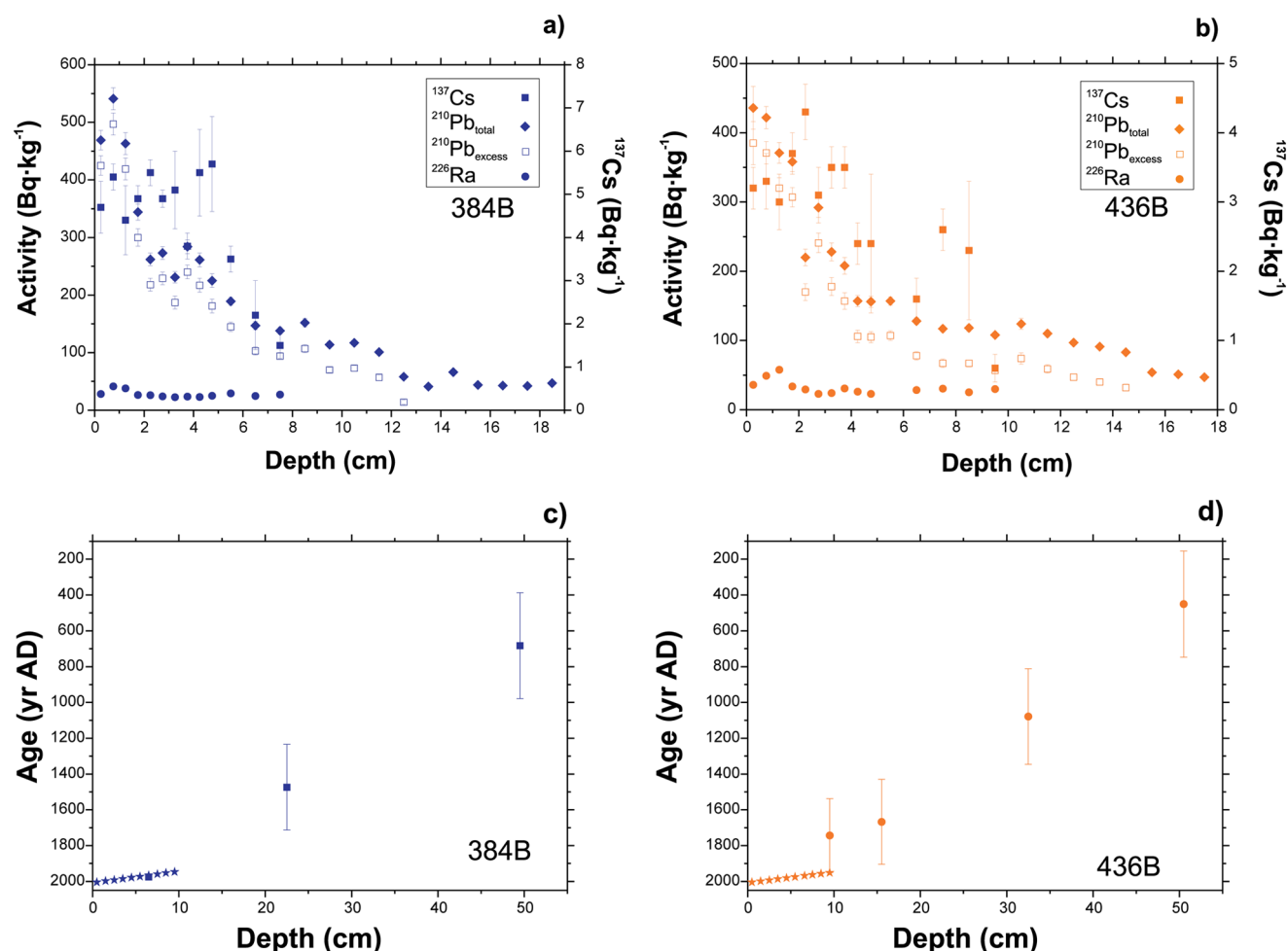
Figure 2. Activity profiles of $^{210}Pb_{excess}$ (open squares), ^{137}Cs (solid squares) and ^{226}Ra (circles) for core 384B (a) and 436B (b) with error bars representing 1σ uncertainties. Final age–depth model including $^{210}Pb_{excess}$ and ^{14}C dates for cores 384B (c) (blue squares) and 436B (d) (orange circles) with error bars representing 2σ uncertainties (colour figure available online).

data set of Levin and Kromer (2004), updated by Levin et al. (2008).

Geochemical, mineralogical and sedimentological analyses

Bulk and clay mineral compositions were obtained by X-ray Diffraction every 1 cm (PANalytical X'Pert PRO diffractometer). Clay fraction separation and sample preparation was performed according to the international recommendations compiled by Kisch (1991). Diffractograms were interpreted using the Xpowder software (Martín, 2004). Peak areas were measured in order to estimate semiquantitative mineral contents, the estimated error being <5% for bulk mineral composition and 5–10% for clay mineral proportions. The reflecting factors calculated for this equipment and its instrument conditions were (1) for powder diffractograms: phyllosilicates, 0.09; quartz, 1.43; calcite, 1.05; feldspar, 1.03; (2) for oriented sample diffractograms: illite, 0.36; chlorite, kaolinite, 0.98; I/S mixed-layer, 0.65 (see Martinez-Ruiz et al., 1999, for details).

Clay mineral characterization was carried out by quantitative geochemical microanalyses every 5 cm using a High-Resolution Transmission Electron Microscopy (TEM) (Philips CM-20 equipped with an EDAX microanalysis system). Additionally, barite was separated from selected samples with higher Ba content by a sequential leaching procedure (Eagle et al., 2003), and morphological analyses of barite were acquired by Field Emission Scanning Electron Microscopy (SEM) (LEO-Carl Zeiss-GEMINI-1530).

Major elements were measured every 1 cm using Wavelength Dispersive X-ray Fluorescence Spectrometry (Bruker AXS S4 Pioneer with an Rh anode X-ray tube) using pressed pellets, with an analytical detection limit of 0.1% and an instrumental error <1%. Trace elements were analyzed by Inductively Coupled Plasma-Mass Spectrometry (Perkin-Elmer Sciex Elan 5000) using Re and Rh as internal standards with an instrumental error of ±2 and ±5% for elemental concentrations of 50 and 5 ppm, respectively (Bea, 1996). Samples were prepared by sequential acid digestion (HNO_3+HF) and measured in triplicate.

TOC content was determined every 1 cm using a Horiba EMIA-320V Series Carbon/Sulfur Analyzer. Ground samples were subjected to acid leaching (HCl) onto glass fiber filters in order to remove inorganic carbon. Treated samples were oxidized by the high-frequency induction furnace method under an oxygen stream, and CO_2 gases evolved were detected by calibrated infrared cells. TOC content was expressed as a percentage of dry weight. The accuracy of the method is 92% and precision is 0.01%.

A granulometric study was undertaken on the bulk fraction at 2 cm intervals, removing the coarse fraction (>63 μm), carbonates and organic matter by wet sieving, treatment with acetic acid and hydrogen peroxide, respectively. Grain size was determined as a cumulative mass percentage using a Micromeritic Sedigraph III 5120. Resolution and accuracy are, respectively, 1 and 0.1 μm. The coarse silt fraction or sortable silt (SS, 10–63 μm), predominantly composed of quartz and feldspar, was considered as an indicator for paleocurrent speed (McCave and Hall, 2006; Rogerson et al., 2008).

Statistical treatment of analytical data was performed using the statistical software package R (Development Core Team, 2011). The normalized geochemical data set was clustered using the complete linkage method (or furthest neighbor method). Redundancy Analyses (RDA) were carried out on the geochemical and the mineralogical data set using the 'vegan' package (Oksanen et al., 2009), and Principal Component Analyses (PCA) and the correlation coefficient of Pearson (r) were performed on the geochemical data set.

Age–depth model and sedimentation rates

$^{210}Pb_{excess}$, ^{226}Ra and ^{137}Cs activity profiles of cores 384B and 436B are shown in Figure 2 and Tables SI and SII available online. The presence of $^{210}Pb_{excess}$ and ^{137}Cs in the first centimeters confirms that the upper part of the records correspond to sediment accumulated during the last century. The maximum ^{210}Pb concentrations are observed at the top of the core and decrease down to 12.5 and 14.5 cm depth for core 384B and 436B, respectively. The maximum sedimentation rates obtained using the Constant Flux:Constant Sedimentation model (CF:CS) are 1.49±0.13 mm/yr for core 384B and 1.41±0.12 mm/yr for core 436B, slightly higher than those derived by Masqué et al. (2003) in sediment cores collected in the same area. The ^{137}Cs activity profile concentrations present maxima concentrations at 4.75 and 2.25 cm for core 384B and 7.5 and 2.25 cm for core 436B, respectively. These maxima correspond to the peak of global fallout because of the nuclear weapons testing in 1963 and the Chernobyl accident in 1986, respectively, and are consistent with an average sedimentation rate of 1.2 and 1.5 mm/yr for cores 384B and 436B, respectively.

^{14}C-derived linear sedimentation rates are 0.33 and 0.36 mm/yr for cores 384B and 436B, respectively, which are four-fold lower than those obtained from the age model derived from ^{210}Pb and ^{137}Cs (Figure 2c, d; Table SIII available online). Differences between the ^{14}C and ^{210}Pb-^{137}Cs derived age models are not surprising in high productivity areas such as the continental margin of the Alboran Sea (e.g. Cochran, 1985; Nittrouer et al., 1984), mainly due to bioturbation effect on the short-lived radionuclides that lead to the estimation of maximum sedimentation rate. Indeed, the presence of some burrows in the upper layers is concomitant with a roughly constant $^{210}Pb_{excess}$ concentration. In addition, reporting results in length per time (mm/yr) rather than mass flux (g/cm² per yr) may bias the interpretation towards high ^{210}Pb-derived ages because the density of surface sediment layers is lower than in deeper layers. Therefore, the age model used in this work is based on the ^{14}C ages although the ^{210}Pb and ^{137}Cs age model on sediment surface constrains it to the 20th century.

Results: Sediment composition, geochemical and sedimentological proxies

Analyzed sediments are predominantly composed of clay minerals (30–70%), calcite (10–30%) and quartz (10–30%), with minor amounts of dolomite and feldspars (<10%). Clay mineral assemblages consist of detrital mica (50–80%), kaolinite (10–25%) and smectites (5–30%) (Figure 3). Additional fibrous clay minerals, such as palygorskite and sepiolite, were identified and characterized by quantitative geochemical microanalyses using TEM, although their content quantified via X-ray Diffraction was below instrumental error (<5%). The same TEM geochemical microanalyses verified that the smectite composition corresponds to Al-rich beidellites, indicating a detrital origin (chemical weathering) and its provenance from soils of the Iberian margin (Martinez-Ruiz et al., 2003; Zúñiga et al., 2007).

Zr is considered as a typical eolian proxy, mainly contained in the zircon lattice. Zircon is enriched in loess and Saharan dust, belonging to the mineral phases chemically resistant to weathering and being mainly carried by wind-blown dust (e.g. Martinez-Ruiz et al., 2000; Wehausen and Brumsack, 1999; see also supplementary material available online for further details). Detrital elemental ratios such as Si/Zr and Zr/Al were calculated, with the aim of enhancing fluvial and eolian fluctuations signals (Figure 4). Zr/Al exhibits higher values at AD 1000–1300 yr, AD 1500–1600 yr, AD 1650–1750 yr and during the second-half of the 20th century. As for Si/Zr ratio, lower values are observed during those time intervals.

Elemental ratios used to infer redox conditions such as V/Cr and Ni/Co ratios were also calculated in order to highlight fluctuations in bottom water currents, in combination with SS and oxygen conditions (Figure 5). These elements provide valuable information on bottom water oxygenation conditions (e.g. Calvert and Pedersen, 2007; Tribovillard et al., 2006; and references therein). Although no significant change is observed in these ratios at site 384B, there is a drastic decrease on the record from site 436B between AD 1470 and 1850 yr and AD 1960 yr onwards (Figure 5).

TOC values vary between 0.7% and 1% at the two sites, displaying a progressive down-core decline (Figure 5) punctuated by relative maxima during the second half of the MCA and the LIA in both cores. The Br/Al ratio mainly mirrors the TOC content trend, supporting a moderate to high correlation between Br and marine organic matter (Ziegler et al., 2008) (Figures 5 and 6; Table SIa and SIb available online) and thus providing a semi-quantitative estimation of sedimentary organic matter.

The grain size distribution consists mostly of clays (50–75%) and fine silts (30–40%) with minor proportions of coarse silt (<15%). Clays are the most abundant grain size at site 384B and fine silt at site 436B. SS values display an uniform pattern in core 384B except at AD 1600–1800 yr when coarser sediments takes place. Core 436B follows a similar trend, with coarser sediments at AD 700–900 yr, AD 1300–1800 yr and during the second-half of the 20th century (Figure 5).

Differences in the location of these sites may have resulted in different processes controlling sediment deposition (Figure 1a). Site 436B is located at the continental slope whereas site 384B is located in a more distal position in the abyssal plain and less affected by direct detrital influx from the platform. Thus, site 384B, would receive a finer fraction while site 436B is more affected by coarser sediments. Grain size distribution of the sediment would, in turn, affect oxygen penetration within the sediment column.

Statistical analyses and interpretation: An insight into paleoclimatic reconstruction

A multivariate statistical strategy has been applied to the mineralogical and geochemical data sets in order to disentangle the main contribution of the different processes controlling sedimentary deposition in the study area. Normalized matrix clustering of the geochemical data and RDA biplots between the geochemical and mineralogical data sets allowed us to identify the main geochemical families and to establish the origin and their relationships with the associated mineral phases, respectively. PCA and Pearson's correlation coefficients have been applied to characterize the major processes affecting the sedimentary regime and the relationship between the variables, respectively (Figure 6).

Two main groups were defined in both cores in accordance to their provenance based on cluster analyses (Figure 6a and b). The first group mainly comprises elements/mineral of typical detrital
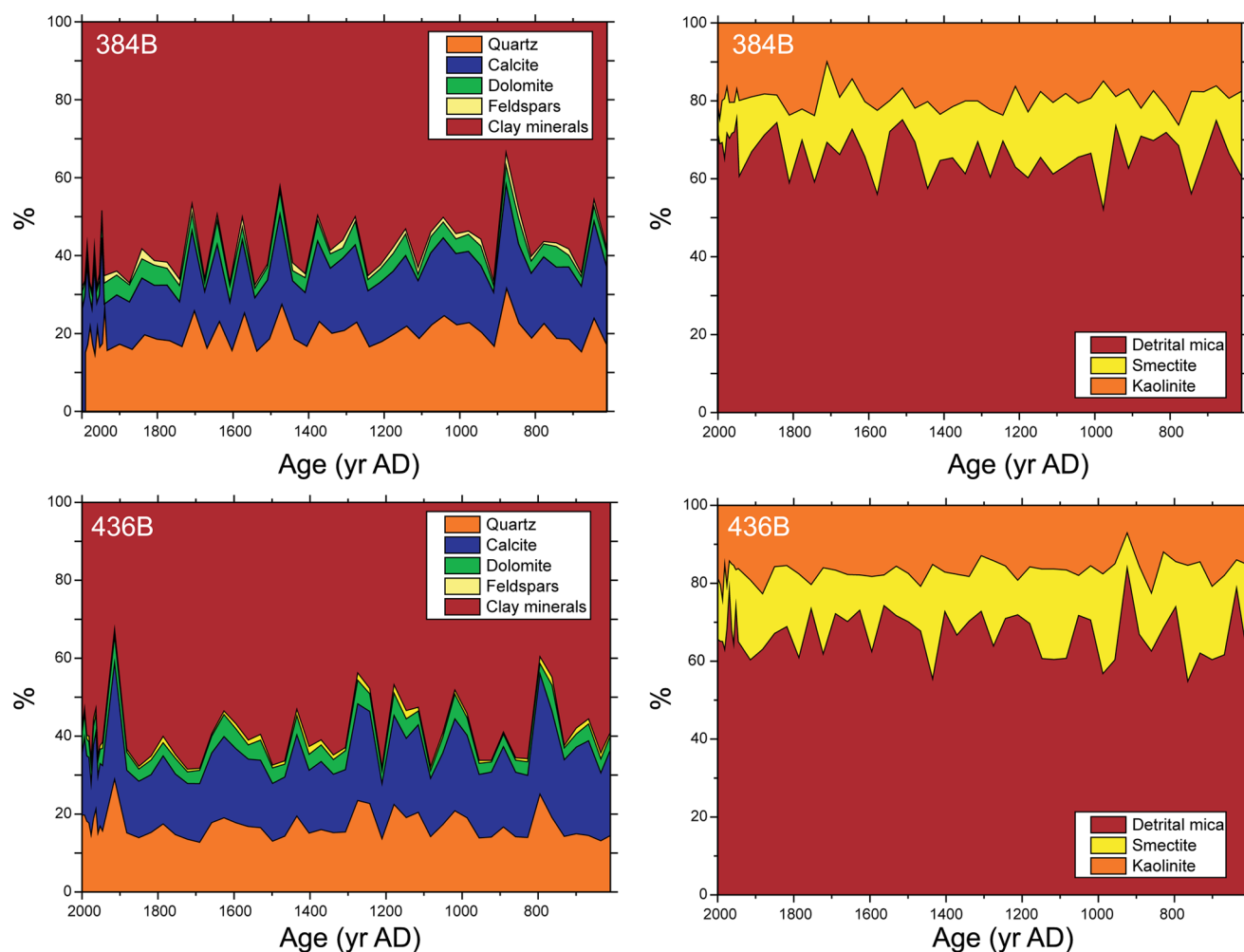
Figure 3. Bulk and clay mineralogy composition (%) for cores 384B and 436B (colour figure available online).
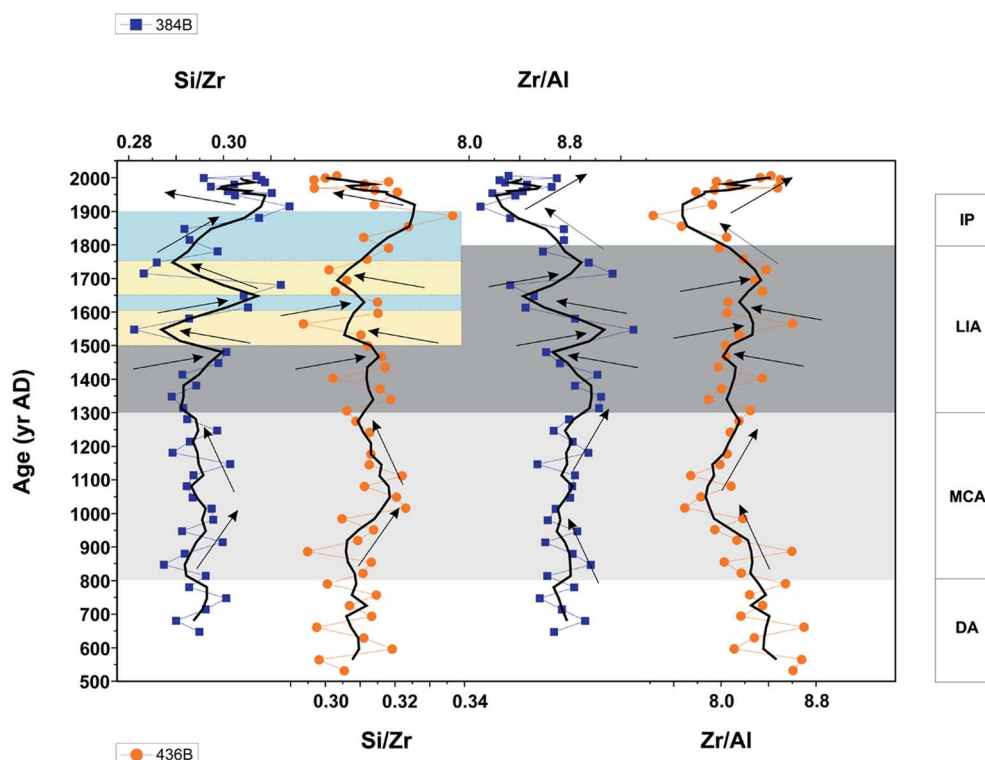
Figure 4. Age–depth profile of detrital proxies (Si/Zr and Zr/Al ratios) for cores 384B (blue squares) and 436B (orange circles). MCA: 'Medieval Climate Anomaly'; LIA: 'Little Ice Age'; DA: 'Dark Ages'; IP: 'Industrial period' (colour figure available online).
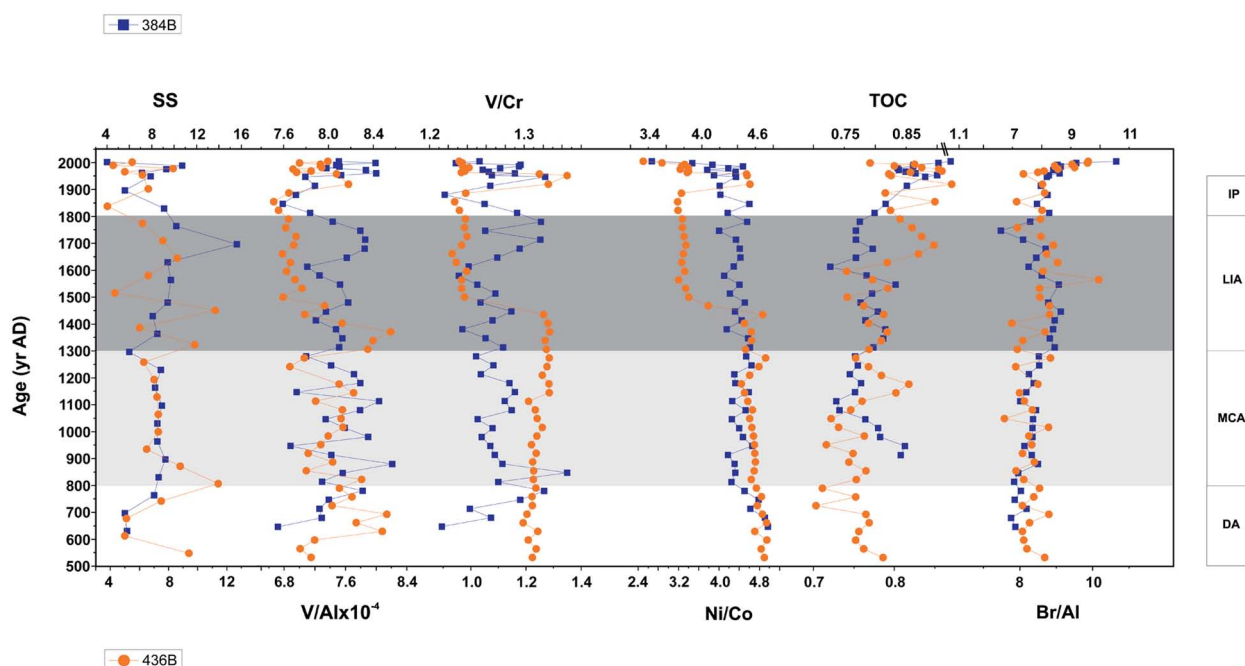
Figure 5. Age–depth profile of grain size distribution (SS, %), redox proxies (V/Al × 10⁻⁴, V/Cr and Ni/Co ratios), and paleoproductivity proxies (TOC content and Br/Al ratios) for cores 384B (blue squares) and 436B (orange circles). MCA: 'Medieval Climate Anomaly'; LIA: 'Little Ice Age'; DA: 'Dark Ages'; IP: 'Industrial period' (colour figure available online).

origin (both fluvial and eolian) and the second group includes elements deposited by processes occurred within the basin, mainly related to carbonate precipitation (Ca, Sr). In both cores, Ba shows a high statistical significance with Rb and REE (Table SIVa and b available online), thus pointing to a detrital origin. Although Ba/Al ratio and biogenic barite have been previously used as paleoproductivity proxies in this region in relation to episodes of enhanced productivity such as the Heinrich events (e.g. Jiménez-Espejo et al., 2008; Rodrigo-Gámiz et al., 2011), within this time interval no Ba excess has been recognized neither biogenic barite was detected. Regarding redox-sensitive elements (V, Cr, Ni, Co, Mo, U and Mn, Table SIVa and b available online), considering the oceanographic setting at the studied sites (intense water masses mixing and strong currents) remarkable changes in redox conditions are unlikely. Indeed, such elements suffer only minor changes (such as V; Figure 5) and TOC display a narrow range of variation (Figure 5), suggesting that sedimentation occurred under oxygenated bottom waters conditions, and only precipitated adsorbed onto clay minerals (Figure 6a and b). Furthermore, U-fixation only occurs under suboxic conditions, that are hardly reachable in this environment, and thus our results evidence the link of U to Ca and Sr, being rather related to carbonate precipitation (e.g. Meece and Benninger, 1993) (Figure 6a, b, c and d). The high correlation between Br and marine organic matter is due to favoured uptake of bromine from seawater by marine plants (e.g. ten Haven et al., 1988; Ziegler et al., 2008) (Table SIVa and b available online). Concerning detrital elements, Ti has been widely interpreted as an eolian proxy. Titanium occurs in accessory Ti-bearing heavy minerals (e.g. rutile, ilmenite or titanite) associated with the coarsest size fraction of eolian sediment (e.g. Nijenhuis et al., 2001; Plewa et al., 2012). In our data set Ti shows good correlation with Zr and a moderate correlation with Al (Figure 6a, and b; Table SIVa and b available online), thus indicating a predominant eolian component with minor fluvial origin. Magnesium and potassium are supplied by chlorite and illite+feldspar respectively of fluvial provenance (e.g. Martinez-Ruiz et al., 2000; Wehausen and Brumsack, 1999). In our data, K also shows a good correlation with Zr and Ti in core 384B (Figure 6a; Table SIVa available online), thus pointing to certain eolian contribution of illite. Mg also shows a mixed behaviour,

being partly associated with carbonates in the form of dolomite and Mg-rich calcite, and partly related to smectites and chlorites of fluvial origin (Figure 6b; Table SIVb available online).

Similarly, RDA biplots display two main groups of chemical elements and associated mineral phases (Figure 6c and d). Group I encompasses detrital mineral phases of fluvial (illite, dolomite, feldspars) and eolian (kaolinite) origin (e.g. Bout-Roumazeilles et al., 2007), associated with the chemical elements previously included in this group, and Group II include mineral phases related to carbonate precipitation. In core 436B, dolomite appears between both groups, suggesting the existence of both authigenic and fluvial-derived dolomite.

The first two eigenvectors of PCA account for 60% of the total variance at site 384B and for 67% at site 436B. The first eigenvector represents 40% of the total variance at site 384B and 55% at site 436B, and is related to the effect of detrital input and productivity, comprising elements such as K, Ti, Zr, Rb, etc., whereas the second eigenvector represents 20% of the total variance at site 384B and 12% at site 436B, and is affected by element fixation in the water column, and mainly includes elements related to carbonate precipitation (Ca, Sr, Mg) (Figure 6e and f). This result agrees with the differences in the location of these sites, which may have resulted in different processes controlling sediment deposition. Site 436B is located close to the influence of fluvial discharge from the Iberian margin and thus more affected by detrital input (Figure 1b). In contrast, site 384B is located in a comparatively more distal offshore position.

Paleoclimate and paleoceanographic conditions during the last two millennia

Considering the statistical discrimination of elements and its interpretation in terms of their origin, we address a reconstruction of the paleoclimatic and paleoceanographic conditions during the last two millennia in the westernmost Mediterranean using these data sets as proxies for detrital input oscillations, oxygenation conditions and paleocurrent intensity.

The oldest part of our record (from AD 500 yr up to AD 800 yr) entails humid conditions at both sites, evidenced by relatively high
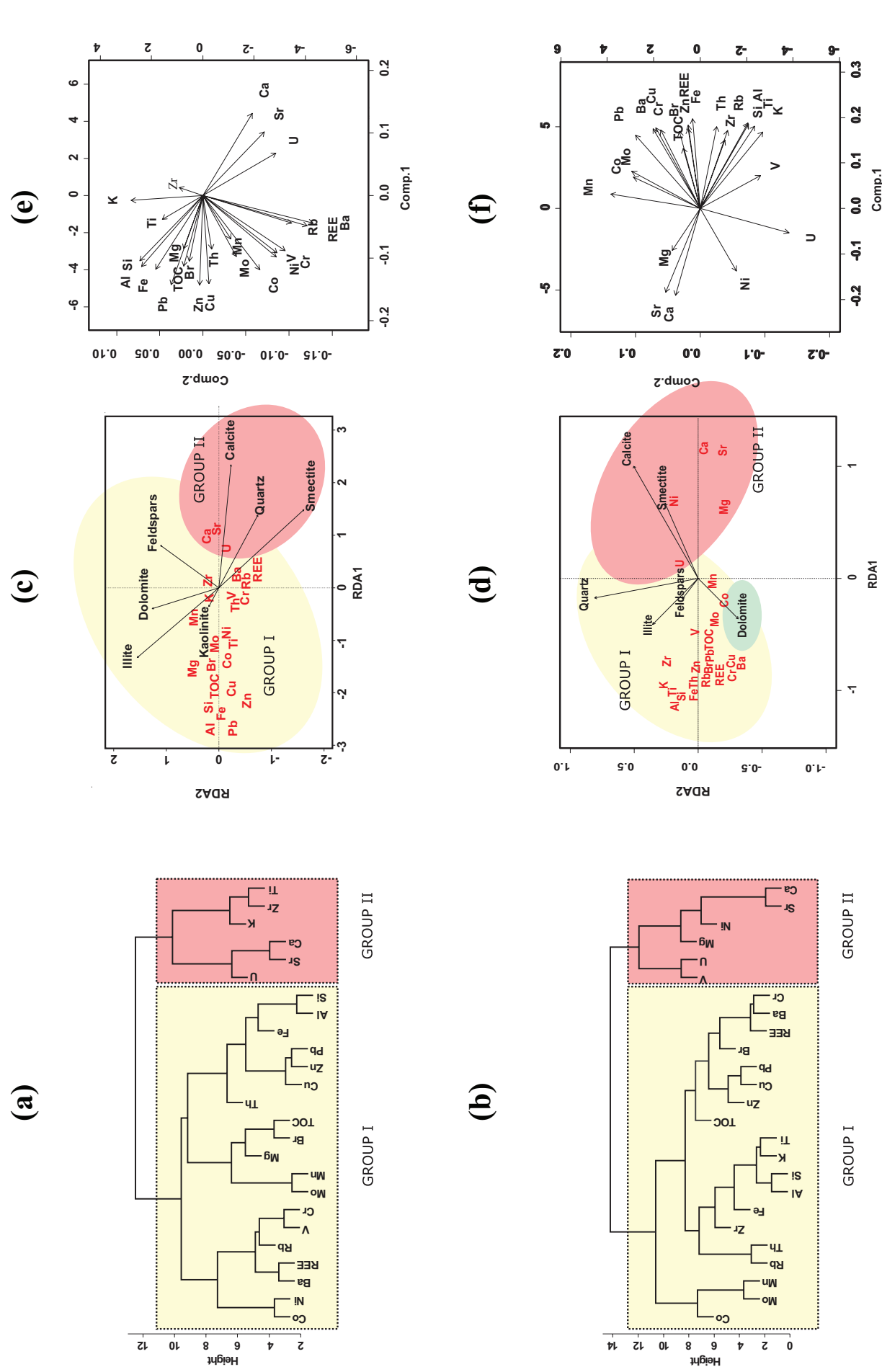
Figure 6. Statistical treatment of data from both sites. Cluster analyses of the geochemical data for sites 384B (a) and 436B (b), and RDA biplots for sites 384B (c) and 436B (d). Light yellow and red areas indicate Group I and II, respectively. Biplots showing the first and the second eigenvector defined by PCA for sites 384B (e) and 436B (f) (colour figure available online).

and constant values of fluvial-derived element (Si/Zr) and a concomitant decrease of the Zr/Al ratio, associated to lower eolian input (Figure 4). The presence of finer grain-size sediments (low SS values) and high redox-sensitive elements values (V/Cr and Ni/Co) indicate relatively low energetic bottom current flows and poor oxygenated bottom waters (Figure 5). Accordingly, TOC content and Br/Al ratios remain stable (Figure 5), thus indicating organic matter preservation because of both detrital input into the basin and slower oxygen replenishment in bottom waters (Figure 4).

Following this period, progressively more humid conditions govern from AD 800 to 1000 yr, thereby higher riverine input into the basin is manifested by a rise in fluvial-derived element (Si/Zr ratio). A concomitant decrease of the Zr/Al ratio also takes place, which indicates lower eolian input (Figure 4). This is followed by prevalent dry conditions as suggested by a declining trend of the fluvial input into the basin (Si/Zr) and higher eolian dust contribution (Zr/Al) in both cores between AD 1000 and 1300 yr (Figure 4). No significant change in paleoceanographic conditions is observed and a moderate hydrodynamic situation is still outlasting as suggested by an essentially fine grain size (low SS values) (Figure 5) and high values of redox-sensitive elements (V/Cr and Ni/Co ratios; Figure 5). Respectively, organic matter is partially preserved (no significant fluctuations of TOC content and Br/Al ratios) (Figure 5), as expected under these conditions of moderate hydrodynamic conditions.

The period between AD 1500 yr and the beginning of the Industrial period (~AD 1800–1950 yr) is depicted by a sequence of short and sharp dry/humid phases characterized by a sudden decrease of fluvial-derived element (Si/Zr) parallel to the eolian input decline in both cores (Zr/Al) occurring at AD 1500–1600 and 1650–1750 yr when drier conditions are observed, while opposite trends are identified at AD 1600–1650 and 1750–1800 yr (Figure 4). A noteworthy change of paleoceanograhic conditions took place at ~AD 1450 yr, lasting until AD 1900 yr. A sudden decrease of redox-sensitive elements in core 436B (V/Cr and Ni/Co ratios) together with higher SS values indicates more energetic bottom currents and better oxygenated bottom waters after AD 1450 yr (Figure 5). This intensification is attributed to an enhancement of the Atlantic jet stream incoming into the Mediterranean Sea because of a weakened North Atlantic Deep Water (NADW) production reported for this period (as much as 10% weaker) (Trouet et al., 2012, and references therein). Cold spells and reduced NADW have been previously invoked to explain fresh polar-derived waters reaching the Alboran basin and flowing into the Mediterranean (Rogerson et al., 2010; Sierro et al., 2005). This current produces an anticyclonic gyre while progressing eastwards into the Mediterranean Sea where site 436B is located (the Western Alboran Gyre, WAG) whose intensification might favour the ventilation caused by the WMDW (Naranjo et al., 2012).

Prevalent humid conditions characterize the recent IP as reflected by a rising trend of fluvial-derived element (Si/Zr). A long-lasting decline of the eolian input (Zr/Al) is also observed in both records (Figure 4). Therefore, even more humid conditions are attained during this period. A return to a moderate hydrodynamic situation, consisting of slower bottom currents and less efficient oxygen penetration in the sediment, is pointed out by low SS values (essentially finer grain-size distribution) (Figure 5) and the slightly more efficient precipitation of redox-sensitive elements in core 436B (V/Cr and Ni/Co ratios; Figure 5). An increasing trend of TOC content and no significant fluctuations of Br/Al ratios in both cores (Figure 5), resulting from higher detrital input and lower oxygenation conditions support this scenario.

The second-half of the 20th century is characterized by a steadily decreasing humidity (as clearly evidenced by fluvial-derived element, Si/Zr) and enhanced eolian input (Zr/Al) (Figure 4). This fact could be related to surface runoff and erosional processes caused by agricultural practices since industrial times.

Our record also exhibits a sudden decrease of redox-sensitive elements in core 436B at ~AD 1950 yr, pointing to a fluctuation into better oxygenated bottom waters (Figure 5), which is supported by raising SS values indicating a sudden re-invigoration of bottom waters currents (Figure 5).

Regional reconstruction and climate connections in the western Mediterranean

Prevailing humid conditions during the time interval represented by the first part of our record (AD 500–800 yr) are characteristic of the period referred as the Dark Ages (DA) (Figure 4). Thus, this phase manifests increasing humidity in the studied area, as evidenced by other records in the western Mediterranean (see Nieto-Moreno et al., 2011, and references therein).

The period encompassing AD 800 to 1300 yr, the MCA, clearly images more humid conditions between AD 800 and 1000 yr, mainly evidenced by enhanced fluvial input (Si/Zr) and rapid decrease in eolian derived element (Zr/Al) (Figure 4). However, an abrupt arid phase is recognized between AD 1000 and 1300 yr as expected for a positive NAO mode (Wanner et al., 2001)(Figure 7), which coincides with the Medieval solar activity maximum (~AD 1100–1250 yr) (Jirikowic and Damon, 1994). Other marine and terrestrial records in the western Mediterranean and the Iberian Peninsula are in agreement with the present record (Martín-Puertas et al., 2010; Moreno et al., 2012; Nieto-Moreno et al., 2011) (Figure 7).

At the end of the MCA and the transition into the LIA, the two studied cores record a period of increase in riverine input (~AD 1300 yr). Then, the LIA (~AD 1300–1800 yr) is characterized as a period of dry–humid phase alternation, showing an increasing trend of fluvial-derived element (Si/Zr) and lower eolian input (Zr/Al) (Figure 4). In this way, Martín-Puertas et al. (2010) and Nieto-Moreno et al. (2011) also found an increase of the riverine input for this period. Moreno et al. (2012) reports high lake levels and mexophytic vegetation, which typically thrive in moderately humid conditions, occurring in the south of the Iberian Peninsula during the LIA (Figure 7). It is also worth mentioning that the humid conditions interpreted from our LIA records coincide with rainfall reconstructions for the last 500 yr on the south of the Iberian Peninsula based on original documentary sources (Rodrigo et al., 1999) (Figure 7). Thus, Rodrigo et al. (1999) inferred prevailing humid anomalies in southern Iberia at AD 1590–1650 yr whereas the driest periods occurred at AD 1500–1590 yr and AD 1650–1750 yr, being AD 1540 and 1750 yr the driest years during the LIA, which are in accord with the present record (Figure 4, blue and yellow bars, colour figure available online). These prevalent humid climatic conditions are consistent with the atmospheric–oceanic situation hypothesized by Trouet et al. (2009) in southern Europe and North Africa, with more low pressure tracking into this region and leading to increased precipitation during negatives phases of the NAO.

These humid conditions continued during most of the IP and into the early 20th century (Figure 4). Humid conditions governed the southern Iberian region as evidenced by data based on instrumental precipitation series at AD 1750–1950 yr (Rodrigo et al., 1999) (Figure 7). A negative mode of the NAO is still persistent during this time interval (Trouet et al., 2009) (Figure 7). The obtained reconstruction is congruent with this general climate scenario.

The second-half of the 20th century is marked by a general decrease in fluvial-derived material in our records (Figure 4), even though intense agricultural activity and deforestation should have induced the opposite as stated before, thus stressing the interpretation of diminished precipitation and humid climate on the region. In this sense, a general decreasing trend of rainfall in the southern Iberian region from 1960 onwards (Rodrigo et al., 1999) and elsewhere in the Iberian Peninsula (e.g. Gallego et al.,

Age (yr AD)	Climatic Events	This study	Other records in the westernmost Mediterranean and the Iberian Peninsula				NAO index
			Martín-Puertas et al. 2010	Nieto-Moreno et al. 2011	Moreno et al. 2012	Rodrigo et al. 1999	Trouet et al. 2009
2000	20th CENTURY	Dry				Dry	Positive
1900	IP	Humid				Humid	Negative
1800		Humid				Humid	
1700		Dry				Dry	
1600	LIA	Humid	Humid	Humid	High lake levels Mexophytic vegetation	Humid	Negative
1500		Dry				Dry	
1400		Humid					
1300							
1200		Dry					
1100	MCA		Dry	Dry	Low lake levels Xerophytic vegetation		Positive
1000							
900		Humid					
800							
700	DA	Humid	Humid	Humid			
600							
500							

Figure 7. Summary of the periods described in this study, their relationship with the main global climatic events, the correlation with episodes defined by other proxies and other authors in the nearby area, and climate forcing mechanisms. MCA: 'Medieval Climate Anomaly'; LIA: 'Little Ice Age'; DA: 'Dark Ages' IP: 'Industrial period'.

2011; Rodrigo and Trigo, 2007) has been also observed during the last century. The recent long wintertime dry conditions over Greenland, southern Europe and the Mediterranean, have been related to the persistent and exceptionally positive mode of the NAO since the early 1980s (the highest positive values of the NAO index recorded since AD 1864 yr) (Hurrell, 1995; Rodó et al., 1997). This positive phase of the NAO (Trouet et al., 2009), which manifests a higher than normal Icelandic low pressure and stronger than average westerlies tracking storminess in a more northerly pathway across middle latitudes, leads to dry winters in the Mediterranean region and northern Africa, northern Canada and Greenland, and humid winters in northern Europe and eastern North America (Trigo et al., 2002; Wanner et al., 2001).

Conclusions

A high-resolution multiproxy approach from two well-dated deep-sea marine records from the Alboran Sea basin has served to decipher natural climate variability and to unravel the forcing mechanisms driving climate change during the last two millennia. According to this approach, prevalent arid conditions depicted the MCA and the second-half of the 20th century as supported by decreasing trends of riverine influence (Si/Zr ratio) and enhanced eolian input (Zr/Al ratio). Meanwhile, the LIA and the IP appeared as prevalent humid periods characterized by opposite trends, which is in agreement with instrumental precipitation series in the south of the Iberian Peninsula. Our climatic records also evidence correlation with other late-Holocene marine records from the westernmost Mediterranean and with lacustrine and pollen records from the south of the Iberian Peninsula. This supports the link between the climate on this region and the North Atlantic realm, driven by the atmospheric forcing related to the NAO. Paleoceanographic fluctuations have also been evidenced at AD 1450 and 1950 yr by a sharpened decrease of redox-sensitive elements (V/Cr and Ni/Co ratios) and coarser sortable silt, which suggest intense circulation of bottom waters as well as a plausible strengthened cold spell of the Atlantic jet stream into the Alboran Sea, reinforcing the link between the reduction of NADW and the inflow of Atlantic waters into the Mediterranean Sea.

References

Bea F (1996) Residence of REE, Y, Th and U in granites and crustal protoliths; implications for the chemistry of crustal melts. *Journal of Petrology* 37: 521–552.

Bethoux JP (1979) Budgets of the Mediterranean Sea: Their dependence on the local climate and on the characteristics of the Atlantic waters. *Oceanologica Acta* 2: 157–163.

Bout-Roumazeilles V, Combourieu Nebout N, Peyron O et al. (2007) Connection between South Mediterranean climate and North African atmospheric circulation during the last 50,000 yr BP North Atlantic cold events. *Quaternary Science Reviews* 26: 3197–3215.

Bradley RS and Jones PD (1993) 'Little Ice Age' summer temperature variations: Their nature and relevance to recent global warming trends. *The Holocene* 3: 367–376.

Bradley RS, Briffa KR, Cole J et al. (2003) The climate of the last millenium. In: Alverson KD, Bradley RS and Pedersen TF (eds) *Paleoclimate, Global Change and the Future*. Berlin, Heidelberg, New York: Springer-Verlag, pp. 105–148.

Calvert SE and Pedersen TF (2007) Elemental proxies for palaeoclimatic and palaeoceanographic variability in marine sediments: Interpretation and application. In: Hillaire-Marcel C and Vernal AD (eds) *Proxies in Late Cenozoic Paleoceanography*. Amsterdam: Elsevier, pp. 567–644.

Cochran JK (1985) Particle mixing rates in sediments of the eastern equatorial Pacific: Evidence from ^{210}Pb, ^{239,240}Pu and ^{137}Cs distributions at MANOP sites. *Geochimica et Cosmochimica Acta* 49: 1195–1210.

Development Core Team R (2011) R: A language and environment for statistical computing. Available at: http://www.R-project.org.

Eagle M, Paytan A, Arrigo KR et al. (2003) A comparison between excess barium and barite as indicators of carbon export. *Paleoceanography* 18(1): 1021.

Fagan (2000) *The Little Ice Age: How Climate Made History, 1300–1850*. Basic Books, New York (USA).

Gallego MC, Trigo RM, Vaquero JM et al. (2011) Trends in frequency indices of daily precipitation over the Iberian Peninsula during the last century. *Journal of Geophyical Research* 116: D02109.

Graham N, Ammann C, Fleitmann D et al. (2011) Support for global climate reorganization during the 'Medieval Climate Anomaly'. *Climate Dynamics* 37: 1217–1245.

Hughes MK and Diaz HF (1994) Was there a 'Medieval Warm Period', and if so, where and when? *Climatic Change* 26: 109–142.

Hurrell JW (1995) Decadal trends in the North Atlantic Oscillation: Regional temperatures and precipitation. *Science* 269: 676–679.

Jiménez-Espejo FJ, Martínez-Ruiz F, Rogerson M et al. (2008) Detrital input, productivity fluctuations, and water mass circulation in the westernmost Mediterranean Sea since the Last Glacial Maximum. *Geochemistry, Geophysics, Geosystems* 9: Q11U02.

Jirikowic JL and Damon PE (1994) The medieval solar activity maximum. *Climatic Change* 26: 309–316.

Jones PD, Briffa KR, Osborn TJ et al. (2009) High-resolution palaeoclimatology of the last millennium: A review of current status and future prospects. *The Holocene* 19: 3–49.

Jones PD, Osborn TJ and Briffa KR (2001) The evolution of climate over the Last Millennium. *Science* 292: 662–667.

Kisch HJ (1991) Illite crystallinity: Recommendations on sample preparation, X-ray diffraction settings, and interlaboratory samples. *Journal of Metamorphic Geology* 9: 665–670.

Lamb HH (1965) The early medieval warm epoch and its sequel. *Palaeogeography, Palaeoclimatology, Palaeoecology* 1: 13–37.

Levin I and Kromer B (2004) The tropospheric (CO$_2$)-C-14 level in mid-latitudes of the Northern Hemisphere (1959–2003). *Radiocarbon* 46: 1261–1272.

Levin I, Hammer S, Kromer B et al. (2008) Radiocarbon observations in atmospheric CO$_2$: Determining fossil fuel CO$_2$ over Europe using Jungfraujoch observations as background. *Science of the Total Environment* 391: 211–216.

Mann ME, Zhang Z, Hughes MK et al. (2008) Proxy-based reconstructions of hemispheric and global surface temperature variations over the past two millennia. *Proceedings of the National Academy of Sciences* 105: 13252–13257.

Mann ME, Zhang Z, Rutherford S et al. (2009) Global signatures and dynamical origins of the Little Ice Age and Medieval Climate Anomaly. *Science* 326: 1256–1260.

Martín-Puertas C, Jiménez-Espejo F, Martinez-Ruiz F et al. (2010) Late Holocene climate variability in the southwestern Mediterranean region: An integrated marine and terrestrial geochemical approach. *Climate of the Past* 6: 807–816.

Martín JD (2004) *Using XPowder: A software package for Powder X-Ray diffraction analysis*. Spain.

Martinez-Ruiz F, Comas MC and Alonso B (1999) Mineral associations and geochemical indicators in the upper Miocene to Pleistocene sediments in the Alboran basin. In: Zahn R, Comas MC, Klaus A (eds) *Proceedings of the Ocean Drilling Program, Scientific Results*, 161: 21–36.

Martinez-Ruiz F, Kastner M, Paytan A et al. (2000) Geochemical evidence for enhanced productivity during S1 sapropel deposition in the eastern Mediterranean. *Paleoceanography* 15: 200–209.

Martinez-Ruiz F, Paytan A, Kastner M et al. (2003) A comparative study of the geochemical and mineralogical characteristics of the S1 sapropel in the western and eastern Mediterranean. *Palaeogeography, Palaeoclimatology, Palaeoecology* 190: 23–37.

Masqué P, Fabres J, Canals M et al. (2003) Accumulation rates of major constituents of hemipelagic sediments in the deep Alboran Sea: A centennial perspective of sedimentary dynamics. *Marine Geology* 193: 207–233.

McCave IN and Hall IR (2006) Size sorting in marine muds: Processes, pitfalls, and prospects for paleoflow-speed proxies. *Geochemistry, Geophysics, Geosystems* 7: Q10N05.

Meece DE and Benninger LK (1993) The coprecipitation of Pu and other radionuclides with CaCO$_3$. *Geochimica et Cosmochimica Acta* 57: 1447–1458.

Millot C (1999) Circulation in the Western Mediterranean Sea. *Journal of Marine Systems* 20: 423–442.

Millot C (2008) Short-term variability of the Mediterranean in- and out-flows. *Geophysical Research Letters* 35: L15603.

Moreno A, Pérez A, Frigola J et al. (2012) The Medieval Climate Anomaly in the Iberian Peninsula reconstructed from marine and lake records. *Quaternary Science Reviews* 43: 16–32 .

Naranjo C, García Lafuente J, Sánchez Garrido JC et al. (2012) The Western Alboran Gyre helps ventilate the Western Mediterranean Deep Water through Gibraltar. *Deep Sea Research Part I: Oceanographic Research Papers* 63: 157–163.

Nieto-Moreno V, Martinez-Ruiz F, Giralt S et al. (2011) Tracking climate variability in the western Mediterranean during the Late Holocene: A multiproxy approach. *Climate of the Past* 7: 1395–1414.

Nieto-Moreno V, Martinez-Ruiz F, Willmott V et al. (2013) Climate conditions in the westernmost Mediterranean over the last two millenia: A biomarker approach. *Organic Geochemistry* 55: 1–10.

Nijenhuis IA, Becker J and De Lange GJ (2001) Geochemistry of coeval marine sediments in Mediterranean ODP cores and a land section: Implications for sapropel formation models. *Palaeogeography, Palaeoclimatology, Palaeoecology* 165: 97–112.

Nittrouer CA, DeMaster DJ, McKee BA et al. (1984) The effect of sediment mixing on Pb-210 accumulation rates for the Washington continental shelf. *Marine Geology* 54: 201–221.

Oksanen J, Kindt R, Legendre P et al. (2009) Vegan: Community Ecology. Available at: http://cran.r-project.org/web/packages/vegan/index.html.

Perkins H, Kinder T and Violette PL (1990) The Atlantic inflow in the Western Alboran Sea. *Journal of Physical Oceanography* 20: 242–263.

Plewa K, Meggers H, Kuhlmann H et al. (2012) Geochemical distribution patterns as indicators for productivity and terrigenous input off NW Africa. *Deep Sea Research Part I: Oceanographic Research Papers* 66: 51–66.

Reimer PJ, Baillie MGL, Bard E et al. (2009) INTCAL09 and MARINE09 Radiocarbon age calibration curve, 0–50000 years cal BP. *Radiocarbon* 51: 1111–1150.

Reimer PJ, Brown TA and Reimer RW (2004) Discussion: Reporting and calibration of post-bomb C-14 data. *Radiocarbon* 46: 1299–1304.

Rodó X, Baert E and Comín FA (1997) Variations in seasonal rainfall in Southern Europe during the present century: Relationships with the North Atlantic Oscillation and the El Niño-Southern Oscillation. *Climate Dynamics* 13: 275–284.

Rodrigo FS and Trigo RM (2007) Trends in daily rainfall in the Iberian Peninsula from 1951 to 2002. *International Journal of Climatology* 27: 513–529.

Rodrigo FS, Esteban-Parra MJ, Pozo-Vázquez D et al. (1999) A 500-year precipitation record in Southern Spain. *International Journal of Climatology* 19: 1233–1253.

Rodrigo-Gámiz M, Martinez-Ruiz F, Jiménez-Espejo FJ et al. (2011) Impact of climate variability in the western Mediterranean during the last 20,000 years: Oceanic and atmospheric responses. *Quaternary Science Reviews* 30: 2018–2034.

Rogerson M, Cacho I, Jiménez-Espejo F et al. (2008) A dynamic explanation for the origin of the western Mediterranean organic-rich layers. *Geochemistry, Geophysics, Geosystems* 9: Q07U01.

Rogerson M, Colmenero-Hidalgo E, Levine RC et al. (2010) Enhanced Mediterranean-Atlantic exchange during Atlantic freshening phases. *Geochemistry, Geophysics, Geosystems* 11: Q08013.

Rogerson M, Colmenero-Hidalgo E, Levine RC et al. (2010) Enhanced Mediterranean–Atlantic exchange during Atlantic freshening phases. *Geochemistry, Geophysics, Geosystems* 11: Q08013.

Ruddiman WF, Kutzbach JE and Vavrus SJ (2011) Can natural or anthropogenic explanations of late-holocene CO$_2$ and CH$_4$ increases be falsified? *The Holocene* 21: 865–879.

Sánchez-Cabeza J, Masqué P and Ani-Ragolta I (1998) ^{210}Pb and ^{210}Po analysis in sediments and soils by microwave acid digestion. *Journal of Radioanalytical and Nuclear Chemistry* 227: 19–22.

Seager R, Graham N, Herweijer C et al. (2007) Blueprints for Medieval hydro-climate. *Quaternary Science Reviews* 26: 2322–2336.

Sierro FJ, Hodell DA, Curtis JH et al. (2005) Impact of iceberg melting on Mediterranean thermohaline circulation during Heinrich events. *Paleoceanography* 20: PA2019.

Stine S (1994) Extreme and persistent drought in California and Patagonia during medieval time. *Nature* 369: 546–549.

Stuiver M and Reimer PJ (1993) Extended C-14 database and revised Calib 3.0 C-14 age calibration program. *Radiocarbon* 35: 215–230.

ten Haven HL, de Leeuw JW, Schenck PA et al. (1988) Geochemistry of Mediterranean sediments. Bromine/organic carbon and uranium/organic carbon ratios as indicators for different sources of input and post-depositional oxidation, respectively. *Organic Geochemistry* 13: 255–261.

Tribovillard N, Algeo TJ, Lyons T et al. (2006) Trace metals as paleoredox and paleoproductivity proxies: An update. *Chemical Geology* 232: 12–32.

Trigo RM, Osborn TJ and Corte-Real JM (2002) The North Atlantic Oscillation influence on Europe: Climate impacts and associated physical mechanisms. *Climate Research* 20: 9–17.

Trouet V, Esper J, Graham NE et al. (2009) Persistent positive North Atlantic Oscillation mode dominated the Medieval Climate Anomaly. *Science* 324: 78–80.

Trouet V, Scourse JD and Raible CC (2012) North Atlantic storminess and Atlantic Meridional Overturning Circulation during the last millennium: Reconciling contradictory proxy records of NAO variability. *Global and Planetary Change* 84–85: 48–55.

Wanner H, Bronnimann S, Casty C et al. (2001) North Atlantic Oscillation - Concepts and studies. *Surveys in Geophysics* 22: 321–382.

Wehausen R and Brumsack HJ (1999) Cyclic variations in the chemical composition of eastern Mediterranean Pliocene sediments: A key for understanding sapropel formation. *Marine Geology* 153: 161–176.

Ziegler M, Jilbert T, de Lange GJ et al. (2008) Bromine counts from XRF scanning as an estimate of the marine organic carbon content of sediment cores. *Geochemistry, Geophysics, Geosystems* 9: Q05009.

Zúñiga D, García-Orellana J, Calafat A et al. (2007) Late Holocene fine-grained sediments of the Balearic Abyssal Plain, Western Mediterranean Sea. *Marine Geology* 237: 25–36.